Demonstration of a 6-4 State Reference Frame Independent channel for Quantum Key Distribution

Ramy Tannous,[1,*] Zhangdong Ye,[1,2] Jeongwan Jin,[1] Katanya B. Kuntz,[1] Norbert Lütkenhaus,[1] and Thomas Jennewein[1,3]

[1]*Institute for Quantum Computing, Department of Physics and Astronomy, University of Waterloo, Waterloo, Ontario, N2L 3G1 Canada*

[2]*State Key Laboratory of Low-Dimensional Quantum Physics and Department of Physics, Tsinghua University, Beijing 100084, China*

[3]*Quantum Information Science Program, Canadian Institute for Advanced Research, Toronto, Ontario, M5G 1Z8 Canada*

(Dated: November 6, 2022)

We propose and demonstrate a novel protocol for reference frame independent quantum key distribution using six states for Alice and four states for Bob. We show that this protocol can generate a secure key for any possible phase of the entangled state, as long as the variation is small compared to the measurement run, despite the reduced four state measurement in Bob's polarization state analyzer. We perform a proof-of-principle experiment using polarization entangled photon pairs. Despite a rotational phase, we obtain a consistently low error rate of less than 3% indicating the feasibility of this protocol for quantum key distribution. Our protocol is beneficial but not limited to applications in satellite or mobile free-space QKD, where the remote communication node must limit resources and restrict the number of measured states to four instead of six.

I. INTRODUCTION

Quantum key distribution (QKD) protocols provide a means of generating and sharing an encryption key between two parties, Alice and Bob, with the security guaranteed by the laws of quantum physics [1]. There is an on-going effort to improve the practicality and robustness of QKD [1]. In many protocols, both Alice and Bob need continuous agreement of all shared measurement frames during the entire period of communication [2–4]. The definition of the measurement frames is essential for key generation, for instance protocols that utilize polarization encoding, a geometric reference is required. However, this demand can be relaxed by employing reference frame independent (RFI) protocols, that allows all or some of the measurement frames to freely to rotate by some slowly varying relative phase ϕ[5–7]. RFI protocols are useful in many settings such as free-space satellite links where the frames of reference may not be maintained due to rotations of the satellite[5].We present and implement a RFI protocol, using polarization entangled photons, where one receiver (Bob) can only perform measurements in two Pauli bases, while the other receiver (Alice) can measure in the usual three Pauli bases, the 6-4 state protocol. Despite the reduced measurement at Bob, we demonstrate that the protocol is still RFI and suitable for QKD.

We experimentally demonstrate the viability of the 6-4 protocol by compensating for the polarization rotations present in optical fibers due to manufacturing tolerances, and thermal and mechanical stress. These rotations are indeed a major challenge for many photonic applications, and one of the major reasons that polarization qubits are rarely used in optical fiber-based quantum channels. Methods to mitigate the rotations caused in optical fibers typically require the isolation and stabilization of the fiber, or the use of active optics to compensate for polarization fluctuations[8]. Polarization maintaining fibers (PMF) were developed to specifically combat these rotations [9], however any polarization not aligned to one of the two axes (slow or fast axis) will be subject to a large birefringent phase, which will typically cause entangled photons to decohere. However, by using our RFI protocol, one can still use PMF for quantum information purposes despite the large birefringent phase that is induced to superposition bases, (i.e. linear combinations of the slow and fast axis polarizations).

TABLE I: Polarization basis with the corresponding Pauli spin matrix and the symbols used in this work.

Basis	Pauli Spin Operator	Symbol
H/V	σ_z	Z
D/A	σ_x	X
R/L	σ_y	Y

A. Protocol

For the 6-4 RFI QKD protocol, we modify the scheme presented by Laing et al.[5] to account for the reduced measurement on Bob's qubit. Alice and Bob share an entangled state ρ_{AB}, each making Pauli measurements on half of the two-qubit state. In our case, the computational basis is the horizontal-vertical polarization basis (Z) which in turn is the fixed basis. Alice applies a 6 state measurement on her qubit, measuring in the Pauli Z, X, and Y bases, while Bob applies a 4 state measurement on his qubit in the Pauli Z, and X bases. Here the Pauli Matrices corresponds to the polarization basis as in Table I.

The reduced measurement at the receiver (Bob) brings several benefits. Most importantly, it reduces the resources required for Bob's state analyzer, which is important for receivers that are constrained by resources such as on satellites like the Quantum Encryption Science Satellite [10] or mobile devices. The omission of the third basis in Bob requires adjusting the parameters used in the symmetric 6 state protocol presented in Laing et al. [5].

We therefore define a phase independent parameter (C-

* ramy.tannous@uwaterloo.ca.

parameter)

$$C = \sqrt{\langle X_A X_B \rangle^2 + \langle Y_A X_B \rangle^2}, \tag{1}$$

where $\langle M \rangle$ is the expectation value of the two qubit positive-operator valued measure (POVM) M, defined as,

$$\langle M \rangle = \frac{M_{++} - M_{+-} - M_{-+} + M_{--}}{\sum_{ij} M_{ij}}. \tag{2}$$

M_{ij} $(i, j = +, -)$ are the coincidence counts of the various results for the POVM M and $\sum_{ij} M_{ij}$ is the total coincidence counts measured of M. By Pauli algebra, we see that $C \leq 1$, with the equality occurring for maximally entangled states. Therefore, the C-parameter effectively provides a second basis that can be useful in a quantum communication context, and will be called the "diagonal*" basis. The C-parameter is used to monitor the quality of the quantum channel and any significant drop from unity can be attributed to an eavesdropper's intervention[5]. C-parameter is a statistical value and it can be shown to be constant even in the presence of a relative phase between the X and Y bases (for both qubits) for a phase that can be approximated as being constant over the finite measurement interval. For example, with the idealized Bell state,

$$|\Psi\rangle = \frac{1}{\sqrt{2}}(|0\rangle_A |1\rangle_B + e^{i\phi} |1\rangle_A |0\rangle_B) \tag{3}$$

we get for $\langle X_A X_B \rangle = \cos(\phi)$ and $\langle Y_A X_B \rangle = \sin(\phi)$. Propagating into Eq. 1, we get $C = \sqrt{\cos(\phi)^2 + \sin(\phi)^2} = 1$, regardless of ϕ. For additional comments on the security also see Laing et al. [5].

The channel integrity is monitored by observing the correlation in both computational and "diagonal*" basis. The quantum bit error ratios (QBER) in the computational basis and the "diagonal*" basis are given by,

$$\begin{aligned} \mathrm{QBER}_{HV} &= \tfrac{1-\langle Z \otimes Z \rangle}{2}, \\ \mathrm{QBER}^*_{Diag} &= \tfrac{1-C}{2}. \end{aligned} \tag{4}$$

In the protocol, both the diagonal and the computational basis are observed to estimate the QBER on the channel, as required for extracting a secure key. The QBER^*_{Diag} is an effective QBER which monitors any drop in the C-value. For a more in-depth analysis of the QBER for RFI protocols, we refer the reader to Yoon et al.[11]. From the estimated QBER an asymptotic key rate is estimated via[12],

$$R \geq Q_\lambda (1 - f H_2(\mathrm{QBER}_{HV}) - H_2(\mathrm{QBER}^*_{Diag})) \tag{5}$$

where Q_λ is the basis reconciliation factor, ($1/6$ in our case), and f is the bidirection error correction efficiency[13, 14], $f = 1$ as we assume error correction at the Shannon limit. It is important to note that the analytical key rate of Eq. 5 does not account for any mismatch in detection efficiencies nor the vacuum or multi photon contributions. We take a more in depth look at this key rate estimation using numerical methods later in Sec. III.

II. EXPERIMENT

The entangled photons used in the experiment are created using a Sagnac interferometer [15] that bidirectionally pumps a periodically poled potassium-titanyl phosphate non-linear crystal that produces type-II spontaneous parametric down conversion with the signal at 776 nm and the idler at 840 nm. Details of the entire experimental setup can be found in Fig 1. The down converted photons are then collected into PMF with the horizontal and vertical polarizations aligned to the two principle axes (slow and fast axis) of the PMF. Thus, the horizontal and vertical polarizations are preserved while any other polarization incident on the fiber will have a random rotational phase due to the difference in index of refraction between the slow and fast axis. The difference in group velocity between the slow and fast component of the polarization will cause temporal displacement, or walk-off.

The entangled photons each travel through 2 m of 780 nm PM fibers. The lengths of the fibers are critical since the walk-off induced to Alice's photons should be the same as Bob's photon. In addition, the walk-off must be less than the pump's coherence time to avoid any distinguishability of the photon pairs, since the coherence time of the entangled photons is transfered from the pump [16, 17]. For our experiment the fibers induce a walk-off of approximately 2.34 ps and the coherence time of the 405 ± 0.005 nm pump is approximately 1.08 ns. The coherence of the pump was closely monitored with a spectrometer, see Fig 1. The pump laser would frequently jump from single-frequency mode to multi-frequency mode operation. It was observed that this reduced the quality of the entangled source and thus the pump spectra was monitored in order to perform our protocol with PMF.

The fibers are rotated by 90° relative to one another since the type-II spontaneous parametric down conversion generated photon pairs with anticorrelated in polarization, to ensure the two photons experience similar walk-offs. The resulting entangled qubit state (ignoring the vacuum component) at the output of the PMF can be approximated to Eq. 3 with ϕ being the phase accumulated from the relative phase between the slow and fast axis of the PMF, Alice and Bob's optical elements and the phase of the pump laser, and $|0(1)\rangle$ is a horizontally (vertically) polarized photon.

After traversing through the PMF the signal is measured by Bob using a free-space 4 state polarization analyzer while the idler is measured by Alice using a free-space 6 state polarization analyzer. All single photon and coincidence counts are measured and recorded using silicon avalanche photodiodes, with detector resolution of 500 ps and a time tagging unit. The coincidences are measured using a 1 ns correlations window and accumulated over a 1 s integration time. It is important to select a correlation window that is larger than the detector resolution as the temporal uncertainty of a photon's arrival is limited by the detector timing jitter. In addition, care was taken to ensure that the optical path efficiency of both state analyzers are similar. However, the detection efficiencies may vary between all the detectors and should be noted as this is a crucial part of our security analysis to follow.

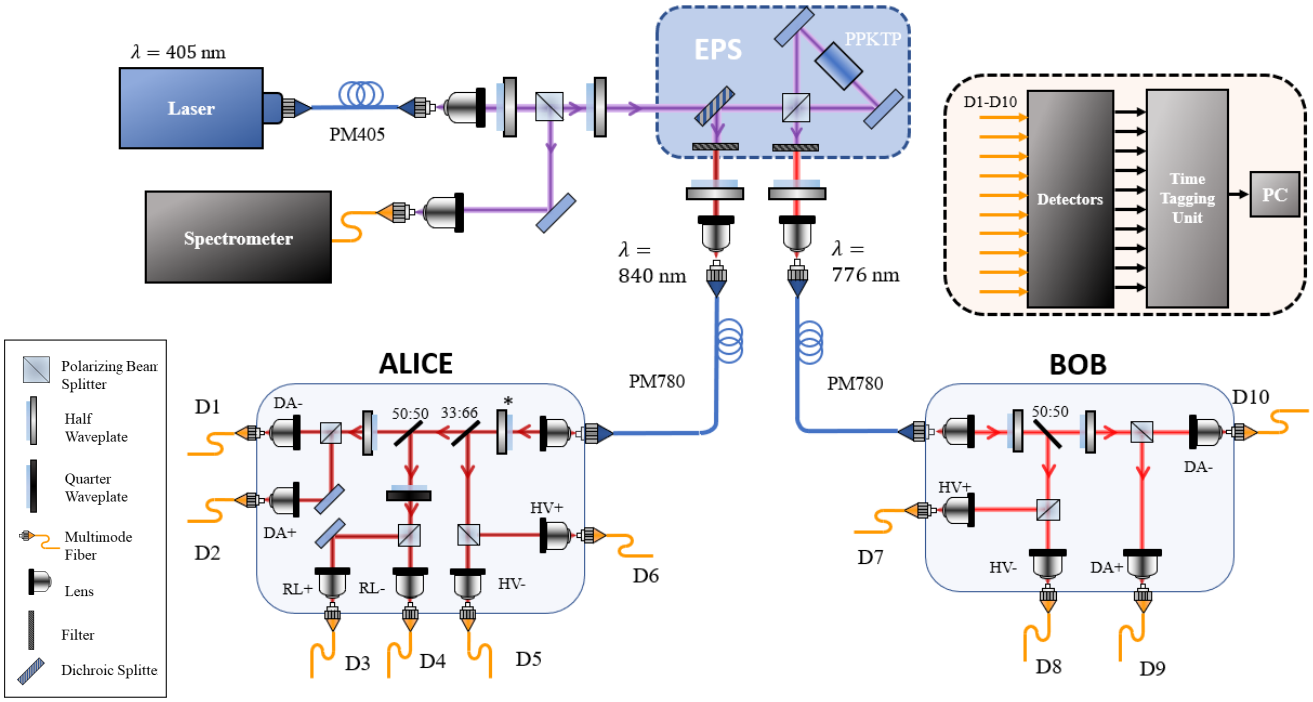

FIG. 1: Experimental setup. A 405 nm laser pumps a type-II periodically poled potassium-titanyl phosphate (PPKTP) non-linear crystal in a Sagnac interferometer[15]. Entangled 776 nm and 840 nm photons are collected into 780 nm polarization maintaining fibers that induce a relative phase between the X and Y bases. Alice performs a complete six state measurement on the 840 nm photon, while Bob performs a tomographically incomplete four state measurement on the 776 nm photon. Ten silicon avalanche photodiodes are used to detect the photons. Coincidence and single events are recorded and analyzed by a time-tagging unit and a computer. A spectrometer is used to monitor the pump spectra during the measurements. * indicates the half-wave plate rotated about its vertical axis which is used to manipulate the external the phase allowing for rapid phase variations.

III. RESULTS AND DISCUSSIONS

We present the results of two experimental conditions: the first scenario (trial (a)) is where the system was left undisturbed such that the rotational phase is only due to drifts in the birefringence of the PMF. In this configuration, any phase changes can be attributed to stress of the fiber, whether it be thermal or physically induced. The second scenario (trial (b)) phase changes where introduced using an additional birefringent element[18].

From the measurements we compute the expectation values of all the possible POVM's using Eq. 2 and calculate the C-parameter. Indeed for trial (a), the C-parameter appears to be a constant function of the phase, see Fig. 2 (a), as expected from the definition of C, Eq. 1. However, in Fig. 2 (b) we see some variation of C, which can be attributed to a rapid change in the relative phase. This drop in C-parameter is also correlated to a drop in the inferred state purity.

A. QBER and Key Rate Estimates

From the correlation data, the QBER is estimated according to Eq. 4. Note that even with the presence of a random relative phase induced by the fiber and the birefringent element, a low overall QBER is maintained. We calculated the average total QBER of $0.021(6)$ for trial (a) and $0.03(1)$ for trial (b). A total QBER of less than 0.11 is required to perform a secure key transfer for systems based on qubits. Our observed QBER are well below this threshold which indicates this protocol is robust to phase drifts despite the lack of complete measurements.

Given the low overall QBER, an asymptotic normalized key rate (per coincidence) is estimated for both trials using Eq. 5, the results are shown in Fig. 2. The drop in key rate in trial (b) is correlated to the spike in QBER that is exhibited during a rapid phase change, up to approximately $0.7\,\mathrm{rad/s}$. The average key rate value for trial (a) is $0.139(6)$ and $0.13(1)$ for trial (b), while the theoretical limit of the key rate per coincidence of our system, given by Eq. 5, is 0.167.

The analytical estimated key rate given from Eq. 5 only provides an estimation for the final key rate as it does not account for detection efficiency mismatches. To further underline the security of the protocol, we take a closer look at the key rate by taking into account the effects of the different detection efficiencies in the various detection paths on both Alice's and Bob's side. In this scenario, we cannot make a fair sampling assumption. We implement a detailed modeling of the physical set-up, and perform a numerical security analysis along

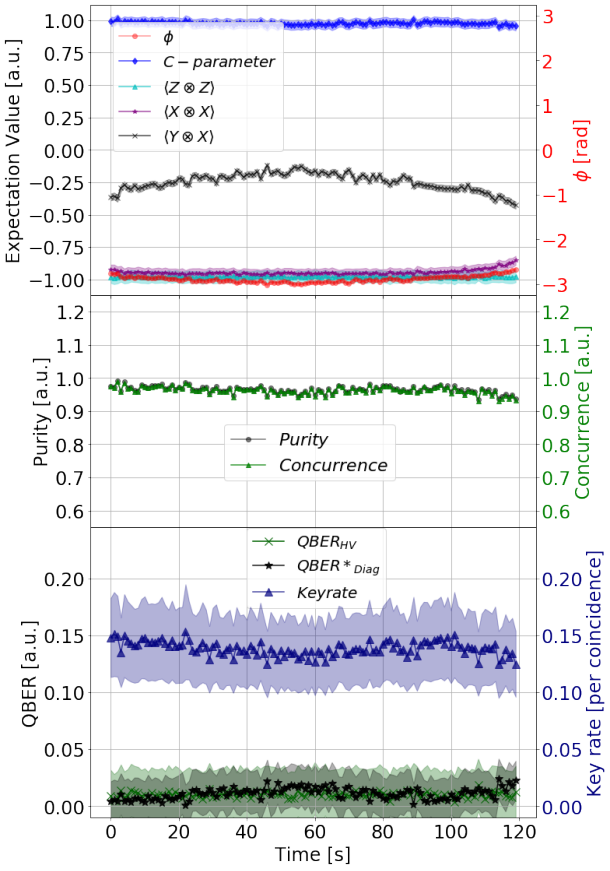

(a) System left undisturbed. Top: the experimental expectation values and phase ϕ. The average C-parameter value is $C = 0.97(1)$. Middle: Purity and concurrence of the entangled state after the transmission through the PM fibers. Bottom: QBER and key rate. The average $QBER^*_{Diag}$ is $0.0112(4)$ and total QBER is $0.021(6)$. The average estimated key is $0.139(6)$. The key rate is the normalized key rate (per coincidence) from Eq. 5.

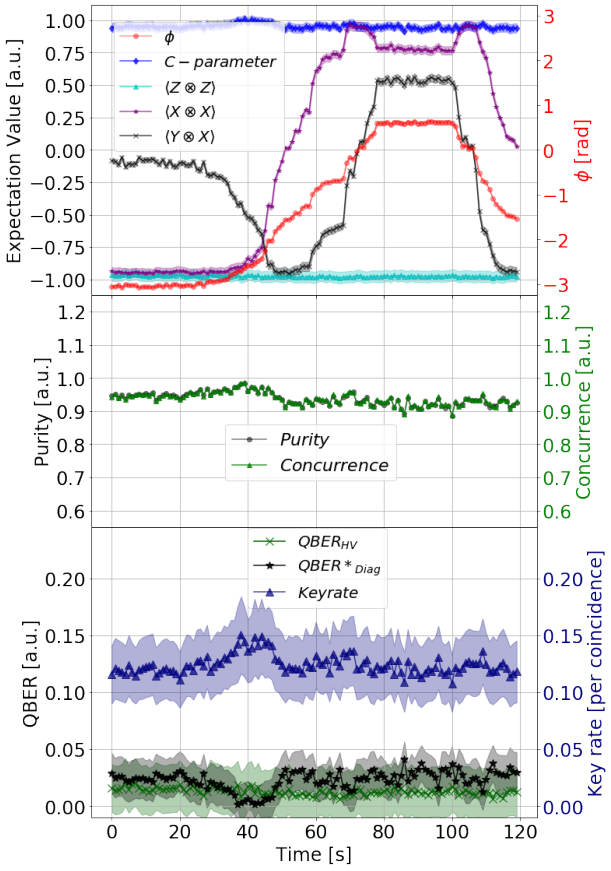

(b) Varying phase induced by a HWP in Alice's analyzer. Top: the experimental expectation values and phase ϕ. The average C-parameter value is $C = 0.96(4)$. Middle: Purity and concurrence of the entangled state after the transmission through the PM fibers. Bottom: QBER and key rate during the phase change. The average $QBER^*_{Diag}$ is $0.022(2)$ and total QBER is $0.03(1)$. The average estimated key rate is $0.13(1)$. The key rate is the normalized key rate (per coincidence) from Eq. 5.

FIG. 2: Experimental results, the shaded regions represent the calculated error in the respective value. Error bounds are present in the top and bottom figures, however, some might be too small to be visible. The error bounds are derived using error propagation of the statistical counting error. No error analysis is provided for the tomographically derived values (purity, concurrence). The key rates in this figure are calculated using the raw coincidence data to compute the various expectation values, (Eq. 2), propagated to compute the QBER, (Eq. 4), which is then used in Eq. 5 to produce the key rates shown above.

the lines of Winick et al. [19].

To accomplish this, we follow three steps. In the first step, we analyze the data to find self-consistent values of the detection efficiencies for the various polarization detection paths. In the second step, we deal with the fact that the experiments provides frequencies of observed events. However, our asymptotic key rate calculation requires probabilities of events. Usually, a rigorous finite size security analysis would work with frequencies, but this is beyond the scope of the current analysis. Instead, we utilize a maximum likelihood approach to convert frequencies to probabilities. In the third step, using the determined detection efficiencies and observation probabilities derived from the quantum state estimation procedure, we perform an asymptotic numerical security analysis.

In our calculations, we assume that the signals in each arm are restricted to vacuum and single photon states in polarization. To facilitate the second step, we impose a time interval structure onto our data to catch the effect of vacuum detections which are extremely predominant due to the enormous amount of clock slots and accordingly shrinks the key rate. Effectively, we assume that the experimental set-up runs on a clock given by time scale of the coincidence detection electronics (1 ns). The effective clock allows us to account for non-detection events properly.

For the first step, we fit the experimental data with a quan-

tum optical model of source and detection, with detection efficiencies as parameter. In this model, we introduce a restriction to vacuum and single photon signals. We verify the self-consistency of this model, use the combined data from all experimental runs and find, for the detection efficiency, fit parameters listed in Table. II. Note that we do not provide an error analysis, as the resulting key rate is only meant as indicator, not as a complete finite size security analysis. Note also that in a proper security analysis, one would have to determine the detection efficiencies in independent calibration measurements that cannot be influenced by the adversary Eve.

For the second step, we use a maximum likelihood method (MLM)[20–22] to reconstruct the joint, two-party density matrix in the respective vacuum and single-photon subspaces in each arm, for the data of each run of the experiment. From the reconstructed density matrix, we use a model of the POVM elements (including the efficiency parameters derived in step 1) to extract probabilities for the observed events. Our selection of the MLM is not restrictive since we are only interested in calculating the density matrix from the experimental data to extract probabilities for the observed events, a task that would usually be taken care of by a full finite size security analysis. The MLM step serves only as a place holder to enable the calculation of asymptotic key rates extrapolated from observed frequencies of events. Therefore, one could also have chosen other tomography methods.

In the third step, we find the asymptotic key rates of the set-up under the model assumptions, following the numerical procedures that are described in detail in Winick et al.[19], which performs a convex optimization procedure over all eavesdropping strategies that are compatible with the observations. We show the resulting key rates for different 20 runs in Figure 3, from which we can see the range of asymptotic key rates that we can expect from the set-up. For the key rate calculation we assume error correction at the Shannon limit.

The results of this detailed analysis, shown in Fig. 3, yield comparable results to that of Eq. 5. Both the more detailed numerical analysis and Eq. 5 yield on the order of 2000 bits/s, the former yielding on average 1750 bits/s (circles in Fig. 3) and the latter yielding approximately 2400 bits/s (triangles in Fig. 3) for the same data. In addition, we perform the following steps to better compare Eq. 5 with our numerical approach. First we take the two-party density matrix that is computed using the MLM and remove the vacuum components to form a two-qubit density matrix. From this two-qubit density matrix, we compute the probabilities for the various experimental events, using our model POVM elements and calculate the QBER as per Eq. 4. From the QBER, we use Eq. 5 to obtain a key rate (square in Fig. 3). In Fig. 3 we see that this method is consistently producing higher key rates (2110 bits/s) than our numerical analysis. Thus, we emphasize that both methods utilize different subsets of the observed data in addition to the different proof assumptions, but the analytical key rate (Eq. 5) with its assumptions overestimates the key rate in this situation. Nonetheless, the numerical analysis which provides the secure key rate determined through a physical model permits us to further underline the security of the 6-4 scheme.

B. State Tomography

From the reconstructed density matrices of the MLM, we discard the vacuum component of each matrix and compute a renormalized two-qubit density matrix. With the new two-qubit density matrices we calculate the quality of the entangled state as a function of time and phase. We quantify the quality of the entanglement using various entanglement measures; purity, fidelity[23] compared to a maximally entangled state of Eq. 3, concurrence[24] and entanglement of formation[24], (Fig. 2, presents the purity and concurrence as a function of time for both trial (a) and (b)). The calculated mean purity for the experimental data is $0.96(1)$ and $0.94(2)$ for trials (a) and (b) respectively, while the mean overlap fidelity with an ideal Bell state of each trial $0.987(3)$ and $0.980(4)$. The fidelities are calculated by comparing the tomographically reconstructed state to Eq. 3, where ϕ is determined from the experimental data and as seen in Fig. 2 (top). The average concurrence is $0.96(1)$ and $0.94(2)$, for trial (a) and (b) respectively, while the average values for entanglement of formation are $0.96(1)$ and $0.92(3)$. As expected, the interesting observation is that the quality of the measured entangled state is relatively stable throughout the phase drift, with the exception during times of rapid phase changes and periods of higher photon loss. Thus, the phase change and effects of the birefringence from the PM fibers have little effect on the quality of the entangled state, therefore enabling the use of the PM fibers in quantum information experiments.

IV. CONCLUSIONS

We demonstrate the feasibility of a novel 6-4 QKD protocol based on entangled photons. Despite the loss of one measurement basis in the receiver, a secret key can be transfered between two parties. The security of the protocol is underlined by performing a numerical analysis of the secret key rate. In addition we have shown that the protocol is reference frame independent and resistant to a relative rotational phase between two of the bases. Furthermore, we demonstrated that polarization entangled photons can be reliably transfered through high birefringence fibers such as polarization maintaining fibers while maintaining a relatively high purity, concurrence and entanglement of formation values. Thus, enabling the use of PM fibers in quantum information experiments. The methods presented are also applicable to enhance many other applications such as polarization compensation systems, quantum LIDAR and metrology. Furthermore, this protocol is applicable to prepare-measure QKD implementations with decoy states, and the additional configuration flexibility for either the sender or the receiver to perform the 6 state operation.

ACKNOWLEDGMENTS

The authors would like to extend gratitude to the funding support from the Canada Foundation for Innovation (CFI),

TABLE II: The ten detector channel efficiencies determined from the experimental data. Superscript A (B) denotes Alice's (Bob's) Detector, while the subscript denotes the particular polarization state associated with that channel.

η_H^A	η_V^A	η_D^A	η_A^A	η_R^A	η_L^A	η_H^B	η_V^B	η_D^B	η_A^B
0.069	0.063	0.076	0.092	0.078	0.073	0.095	0.087	0.120	0.091

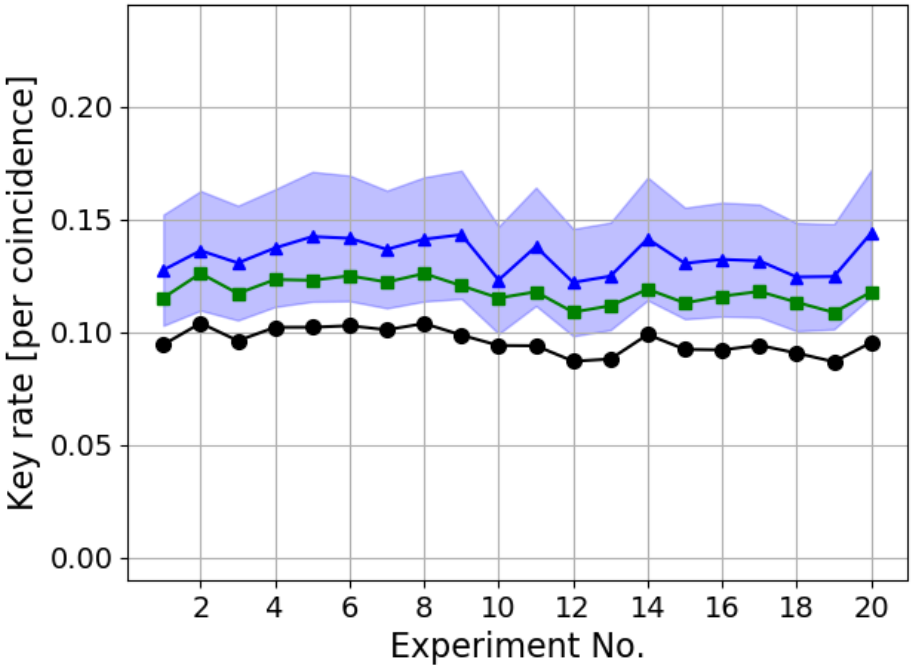

FIG. 3: The normalized key rates (bits per coincidence) of 20 seconds of the experiment. Each point corresponds to data collected over collected over a 1 s integration time. The black circles are determined from the detailed security analysis that includes any detector efficiency mismatch and is a lower bound of the key rate for our protocol. The green squares are calculated from Eq. 5 where the QBER is computed from the single photon probabilities of the density matrices estimated using the MLM. The blue triangles are determined using Eq. 5 using the coincidence counts to compute the expectation values (Eq. 2) and QBER, (Eq. 4). The error bounds for the results of Eq. 5 (triangles), are derived from statistical counting errors. No error analysis is provided for the values derived from the MLM (circles, squares). The discrepancies between the squares and the triangles can be attributed to the MLM used. However, discrepancies between that circles and the squares is independent of the selected state estimation method.

the Ontario Research Fund (ORF), the Canadian Institute for Advanced Research (CIFAR), the Natural Sciences and Engineering Research Council of Canada (NSERC), the Research Collaboration Funding between Tsinghua University and University of Waterloo No. 20173080024, and Industry Canada.

The authors would like to thank Dr. Patrick Coles for initial discussions of the protocol, Kai Hong Li for verifying our calculations, Dr. Sascha Agnes and Kalolina Sedziak for assisting building the experiments, and Dr. Brendon Higgins and Dr. Jean-Phillipe Bourgeoin for insightful discussions on the experiment.

[1] V. Scarani, H. Bechmann-Pasquinucci, N. J. Cerf, M. Dušek, N. Lütkenhaus, and M. Peev, Rev. Mod. Phys. **81**, 1301 (2009).
[2] C. H. Bennett and G. Brassard, in *Proceedings of the IEEE International Conference on Computers, Systems, and Signal Processing* (Bangalore, India, 1984) pp. 175–179.
[3] C. H. Bennett, G. Brassard, and N. D. Mermin, Phys. Rev. Lett. **68**, 557 (1992).
[4] D. Bruß, Phys. Rev. Lett. **81**, 3018 (1998).
[5] A. Laing, V. Scarani, J. G. Rarity, and J. L. O'Brien, Phys. Rev. A **82**, 012304 (2010).
[6] F. M. Spedalieri, Optics communications **260**, 340 (2006).
[7] A. Beheshti, S. Raeisi, and V. Karimipour, arXiv preprint arXiv:1901.01503 (2019).
[8] C. J. Pugh, S. Kaiser, J.-P. Bourgoin, J. Jin, N. Sultana, S. Agne, E. Anisimova, V. Makarov, E. Choi, B. L. Higgins,

and T. Jennewein, Quantum Science and Technology **2**, 024009.
[9] J. Noda, K. Okamoto, and Y. Sasaki, Journal of Lightwave Technology **4**, 1071 (1986).
[10] QEYSsat, `https://uwaterloo.ca/institute-for-quantum-computing/qeyssat` (2018).
[11] J. Yoon, T. Pramanik, B.-K. Park, Y.-W. Cho, S.-Y. Lee, S. Kim, S.-W. Han, S. Moon, and Y.-S. Kim, Optics Communications **441**, 64 (2019).
[12] X. Ma, C.-H. F. Fung, and H.-K. Lo, Phys. Rev. A **76**, 012307 (2007).
[13] G. Brassard and L. Salvail, in *Advances in Cryptology EUROCRYPT'93*, Vol. 765 (1994) pp. 410–23.
[14] N. Lütkenhaus, Physical Review A **61**, 052304 (2000).
[15] T. Kim, M. Fiorentino, and F. N. C. Wong, Phys. Rev. A **73**, 012316 (2006).
[16] M. Shtaif, C. Antonelli, and M. Brodsky, Optics express **19**, 1728 (2011).
[17] G. Kulkarni, P. Kumar, and A. K. Jha, J. Opt. Soc. Am. B **34**, 1637 (2017).
[18] In this case it was a half-wave plate (HWP) rotated about its vertical axis with it's fast axis aligned to the horizontally polarized photons, this is the first HWP found after the output on Alice's side, see * in Fig. 1.
[19] A. Winick, N. Lütkenhaus, and P. J. Coles, Quantum **2**, 77 (2018).
[20] Y. S. Teo, J. Řeháček, and Z. Hradil, Quantum Measurements and Quantum Metrology **1**, 57 (2013).
[21] J. Řeháček, Z. c. v. Hradil, E. Knill, and A. I. Lvovsky, Phys. Rev. A **75**, 042108 (2007).
[22] J. Shang, Z. Zhang, and H. K. Ng, Phys. Rev. A **95**, 062336 (2017).
[23] R. Jozsa, Journal of modern optics **41**, 2315 (1994).
[24] W. K. Wootters, Physical Review Letters **80**, 2245 (1998).
[25] R. Ursin, F. Tiefenbacher, T. Schmitt-Manderbacha, H. Weier, T. Scheidl, M. Lindenthal, B. Blauensteiner, T. Jennewein, J. Perdigues, P. Trojek, B. Oemer, M. Fuerst, M. Meyenburg, J. Rarity, Z. Sodnik, C. Barbieri, H. Weinfurter, and A. Zeilinger., Nature Physics **3**, 481 (2007).
[26] S. Rashleigh, Journal of Lightwave Technology **1**, 312 (1983).
[27] C. Antonelli, M. Shtaif, and M. Brodsky, Phys. Rev. Lett. **106**, 080404 (2011).
[28] J. P. Bourgoin, E. Meyer-Scott, B. L. Higgins, B. Helou, C. Erven, H. Huebel, B. Kumar, D. Hudson, I. D'Souza, R. Girard, *et al.*, New Journal of Physics **15**, 023006 (2013).
[29] D. F. V. James, P. G. Kwiat, W. J. Munro, and A. G. White, Phys Rev A **64**, 052312 (2001).
[30] C. Granade, J. Combes, and D. Cory, New Journal of Physics **18**, 033024 (2016).
[31] C. Granade, C. Ferrie, I. Hincks, S. Casagrande, T. Alexander, J. Gross, M. Kononenko, and Y. Sanders, Quantum **1**, 5 (2017).
[32] N. Gisin, G. Ribordy, W. Tittel, and H. Zbinden, Reviews of modern physics **74**, 145 (2002).
[33] T. Okoshi and K. Oyamada, Electronics Letters **16**, 712 (1980).
[34] R. Stolen, W. Pleibel, and J. Simpson, Journal of Lightwave Technology **2**, 639 (1984).
[35] C. Erven, X. Ma, R. Laflamme, and G. Weihs, New Journal of Physics **11**, 045025.
[36] J.-P. Bourgoin, N. Gigov, B. L. Higgins, Z. Yan, E. Meyer-Scott, A. K. Khandani, N. Lütkenhaus, and T. Jennewein, Phys. Rev. A **92**, 052339 (2015).
[37] A. K. Jha, M. N. O'Sullivan, K. W. C. Chan, and R. W. Boyd, Phys. Rev. A **77**, 021801 (2008).